A whole-body NMR imaging machine

J. Phys. E: Sci. Instrum., Vol. 13, 1980. Printed in Great Britain

A whole-body NMR imaging machine†

J M S Hutchison, W A Edelstein and G Johnson
Department of Bio-Medical Physics and Bio-Engineering, University of Aberdeen, Aberdeen, Scotland, UK

Received 4 February 1980, in final form 11 April 1980

Abstract A nuclear magnetic resonance (NMR) machine capable of producing tomographic sections of the whole human body *in vivo* has been constructed. This system is based on a four coil, air-core electromagnet producing a field of 0·04 T which corresponds to a proton NMR frequency of 1·7 MHz. The images are produced line by line using a selective excitation technique. Magnetic field gradients up to about 5 mT/m are employed. Electronic subsystems are described here including a radiofrequency (RF) amplitude feedback circuit, an RF power amplifier, a transmit/receive switch, a receiver pre-amplifier and gradient coil drivers. For a single scan through a 10^3 mm^3 sample of human muscle tissue *in vivo*, the measured proton density uncertainty is 24% and the spin-lattice relaxation time (T_1) uncertainty is 74%. Phantom images using $CuSO_4$ solution and *in vivo* sections through human chest, thighs and head are presented. T_1 measurements of human muscle, liver and brain tissue *in vivo* give results which agree well with T_1 values for corresponding rabbit tissues measured *in vitro*.

1 Introduction

The possibility of using nuclear magnetic resonance (NMR) techniques for imaging has stimulated considerable activity over the past several years (Lauterbur 1973, Kumar *et al* 1975, Hinshaw 1976, Damadian *et al* 1977, Mansfield *et al* 1978, Hoult 1978, Mallard *et al* 1980, Holland *et al* 1980). Of particular interest are the potential medical applications, where one might make images using NMR measurable parameters such as hydrogen proton density in the water of body tissues or NMR relaxation times of these protons.

We describe here a machine which can produce tomographic section images of the whole human body. We discuss our method of producing images, the physical apparatus, and details of certain electronic components. We also present experimental measurements of the signal-to-noise ratio and consequent imaging spatial resolution, and a number of phantom and human tomographic images. Finally, we describe an experiment using our machine to measure T_1 relaxation times of human tissues *in vivo* and compare them to T_1 relaxation times of rat tissues measured *in vitro*.

† This device is the subject of Patent Applications 25899/78, 40779/78, 79/34864, by the National Research Development Corporation.

2 Imaging method

The imaging principle employed is that of 'selective excitation' (Mansfield *et al* 1976, Hutchison 1976) which uses a spectrally-shaped radiofrequency (RF) pulse in the presence of a field gradient to excite spins in a narrow slice of the three dimensional sample. In the simplest form of this technique, the field gradient is then turned through 90° to a direction parallel to the selected slice, and the spectrum or Fourier transform of the resulting free induction signal then represents the distribution of spins within the slice along the second gradient direction. So far there is no discrimination in the third orthogonal direction, and any image formed is a projection or shadowgraph in this direction.

In order to discriminate in the third direction and achieve true tomographic images, it is necessary to employ a field gradient in this direction along with some selective process. Our method does this by carrying out a selective inversion of spins in the presence of the third gradient prior to the normal selective excitation process sketched above. It is a development of a method proposed in an earlier paper (Sutherland and Hutchison 1978).

To obtain an image line, we collect three separate signals designated S_0, S_1 and S_2. From these, two different signals are derived: $S_A = S_0 - S_1$ contains mainly proton density information whilst $S_B = S_0 - S_2$ contains spin-lattice relaxation time (T_1) information.

We use a coordinate system in which z points in the vertical direction along the static magnetic field, y is horizontal along the long axis of the patient, and x is horizontal at a right angle to y. The origin of the coordinate system is taken to be the intersection of the gradient null planes.

Figure 1 illustrates the gradient and RF pulse sequence actually employed. S_0 is obtained from a basic selective excitation sequence consisting of the events of intervals 3, 4 and 5 only. During interval 3, a spectrally shaped 90° RF pulse is applied along with a gradient G_y^- to excite spins lying in or close to the plane $y = 0$. G_y^+ does not need to have sharp rising or falling edges, or even a flat top; in practice, the waveform approximates to a half cycle of a 250 Hz sine wave, whilst the RF pulse envelope is Gaussian with full width at half maximum (FWHM) 600 μs. Both computer simulation and experiment indicate that this combination gives good slice selection.

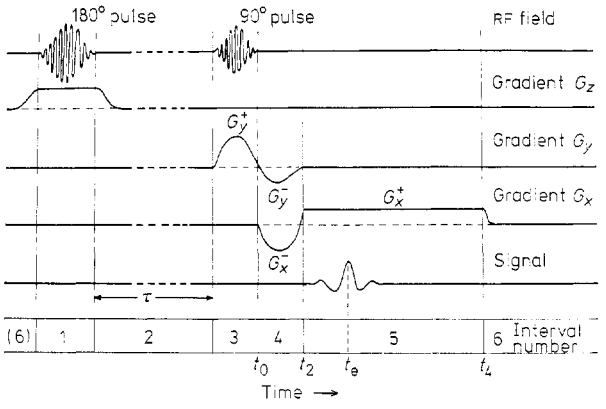

Figure 1 Imaging pulse sequence.

During interval 4, a negative gradient G_y^- is applied to rephase the spins across the slice thickness; this is desirable to obtain the largest possible free induction signal (Hutchison *et al* 1978). Simultaneously, a negative orthogonal gradient

0022-3735/80/090947+09 $01.50

G_x^- is applied to dephase the spins along the slice as a preliminary to collecting the signal.

Interval 5 is the signal collection period, during which a constant, positive gradient G_x^+ is applied. All the spins come into phase in a spin-echo at time t_e such that

$$\int_{t_o}^{t_e} G_x \, dt = 0.$$

In order to discriminate in z and to form an image line running in the x direction, we perform a variation in which the above sequence is closely preceded by a selective inversion. This inversion occurs during interval 1 and consists of a spectrally-shaped 180° RF pulse together with a field gradient G_z. The carrier frequency f_S of the 180° pulse is chosen to selectively invert spins lying in or near the plane

$$z_S = 2\pi \frac{f_S - f_0}{\gamma G_z}$$

where γ is the gyromagnetic ratio ($\gamma/2\pi = 42{\cdot}57$ MHz T^{-1} for protons) and f_0 is the central Larmor frequency. The free induction signal resulting from this process is called S_1.

S_1 differs from S_0 only in the part which is due to spins lying in or close to the intersection of the two planes $y=0$ and $z=z_S$. These spins have been inverted and hence give an antiphase contribution to S_1. If the two signals are subtracted to give $S_A = S_0 - S_1$, then in theory all components should cancel except those arising from spins at the intersection, which should add. The Fourier transform of S_A should then represent the distribution of proton density along x for the line $y=0$, $z=z_S$.

The above procedure can then be carried out a number of times using different values of f_S to give different image lines, and thus build up a complete sectional image. Sufficient time must be given between each pulse sequence to allow the spin system to relax. Ideally one should allow up to five times the longest spin-lattice relaxation time of the sample, which in this case would be about 2 s, but in practice 1 s is enough to give adequate signal definition for regions of different T_1's.

To obtain the third signal S_2, the gap between the 180° pulse and the 90° pulse is increased to something of the order of the average T_1 in the sample. The difference signal $S_B = S_0 - S_2$ now exhibits a much stronger dependence on T_1 because the spins have had time to relax partially after inversion, and S_B can be used to extract T_1 information from the sample. In our apparatus, the interpulse gap τ is 10 ms for S_1 and 200 ms for S_2. Figure 2 shows the theoretical dependence of the amplitude of S_A and S_B on T_1.

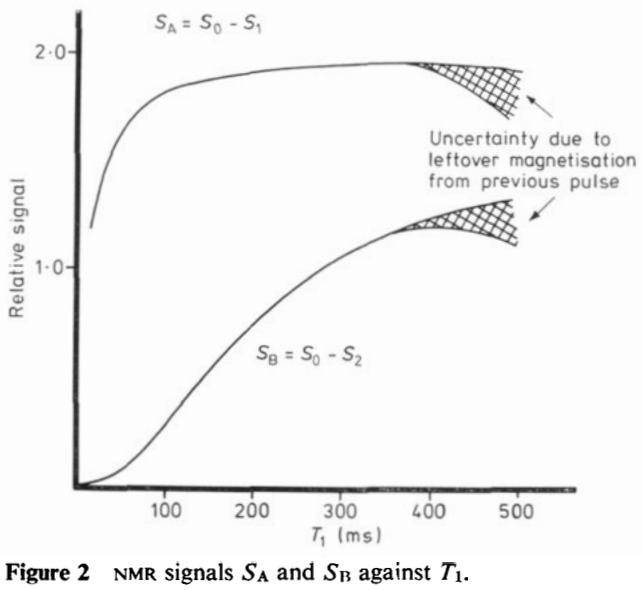

Figure 2 NMR signals S_A and S_B against T_1.

The S_0, S_1 and S_2 sequences are performed as a group of three and f_S is then incremented by 2 kHz in preparation for the next image line. There are 40 lines in one image frame, so that a complete scan takes 2 min.

3 Apparatus

A photograph of the apparatus, taken before completion of the screened enclosure and couch system, is shown in figure 3. One of us (JMSH) is in position for imaging.

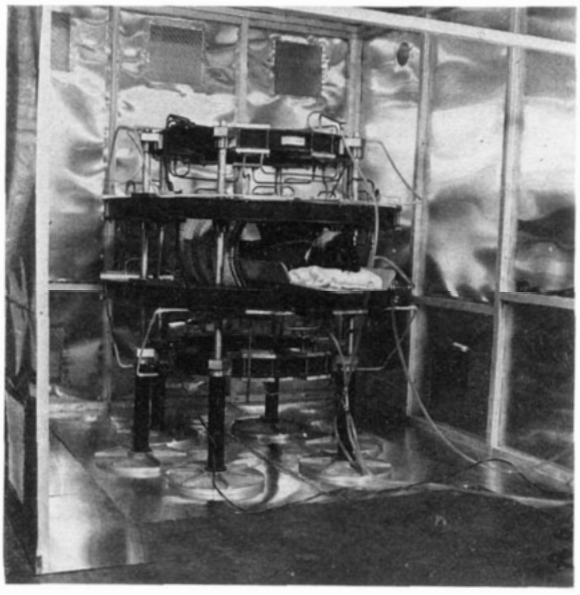

Figure 3 Imaging apparatus.

3.1 *The magnet*

The electromagnet is a four coil system supplied by the Oxford Instrument Company which produces a field of 0·04 T when energised by a current of 40 A from a motor generator. This corresponds to a proton NMR frequency of 1·7 MHz. The two large coils have an average diameter of 1·3 m and are separated by 0·3 m, allowing sufficient space to insert a patient between them. The coil configuration was adjusted in our laboratory to give a homogeneity of around 6×10^{-4} in a central disc 0·46 m in diameter. The magnet is powered by a motor generator and a series regulator with feedback from an NMR probe stabilises the field to about 2×10^{-6}.

3.2 *Field gradient coils*

There are three orthogonal sets of field gradient coils. The four rectangular coils in quadrupolar configuration outside the magnet produce a gradient of about 2·7 mT/m along the axis of the patient (y axis). Gradients along the x and z axes are produced by two windings on the cylindrical former surrounding the patient. The two windings consist of straight wires running axially along the cylinder with a winding density proportional to cos 2θ and sin 2θ respectively. Each winding has 19 wires (1·8 mm diameter) in each quadrant, and the two windings are interlaced so that no adjacent wires are closer than twice their diameter. The windings also act as a Faraday shield for the RF coil wound on the outside of the former (Hutchison *et al* 1979).

3.3 RF *coil*

The RF coil is constructed from 8 mm copper tubing and consists of two 5 turn coils operated in parallel in an electrically balanced mode (figure 7). In conjunction with the Faraday shielding provided by the gradient windings, this configuration gives virtually no electric field inside the cylinder. Each coil is 500 mm in diameter, and the turns are spaced 16 mm apart. The spacing between coil centres is 206 mm, and in the midplane of the apparatus, the RF field in a disc 400 mm in diameter and 20 mm thick has a total variation of 8%. The unloaded Q of the coil was 590 when out of the apparatus, 400 when installed and about 250 with a person inside.

3.4 *Screened enclosure*

The magnet is contained in an electromagnetically screened enclosure constructed from 0·46 mm aluminium sheets nailed onto a 2·4 m cubic wooden frame with copper and brass nails. Electrical connections between adjacent sheets are made with spots of low temperature aluminium solder at 25 mm intervals; this is important because interfering magnetic fields are screened by current loops which flow around the perimeter of the enclosure. The door is a wooden one covered by aluminium sheets with copper spring draught excluder nailed around its edge to make electrical contact when the door is closed.

Filters are installed to prevent electrical interference entering the system via the connections to the magnet and gradient coils. The filters are series resonant circuits tuned to 1·7 MHz and connected between the current leads and the screened enclosure. In most cases these resonant circuits simply consist of 0·22 μF polyester capacitors with the leads trimmed to provide the appropriate inductance.

3.5 *Couch*

An entirely nonmetallic couch has been constructed from expanded polystyrene covered by resin bonded fibreglass and bonded to a thin piece of melamine backed plywood. The couch slides in and out of the sensitive region on Teflon runners.

4 Electronics

A functional block diagram of the system is shown in figure 4. We have developed a number of electronic units which are particularly useful for the present application; these are described below.

4.1 *General*

All control and timing is handled by the central timing and control unit which uses the 1·7 MHz reference quartz oscillator as a master clock. CMOS logic is used throughout, as this offers sufficiently high speed for the purpose and has good noise immunity.

The type of pulse sequence (i.e. S_0, S_1 or S_2) and the image line numbers are specified by an 8 bit word generated on one circuit board and distributed to other units as required. This control word is also converted to serial form and sent via cable to a PDP 11/40 computer some 40 m away which carries out the signal processing as described in §5.1.

Six bits of the control word represent the line number N. The frequency f_S is generated by the synthesiser according to the rule $f_S = 1660 + 2N$ kHz. A CMOS analogue switch (CD4066) is then employed to select either f_S or the reference frequency as the RF source. This signal is passed to the envelope shaping circuits (§4.2) and then through an isolating gate to the power amplifier (§4.3).

A transmit/receive switch (§4.4) has been designed to match the RF sample coil to the power amplifier during pulsing, and to the low noise pre-amplifier (§4.5) during signal acquisition. The main receiver and quadrature detectors are orthodox in design.

The two analogue signals are buffered and sent via coaxial cables to the computer. Each signal goes through a unity gain differential amplifier to overcome ground loop problems and is then band limited by a phase linearised four pole Butter-

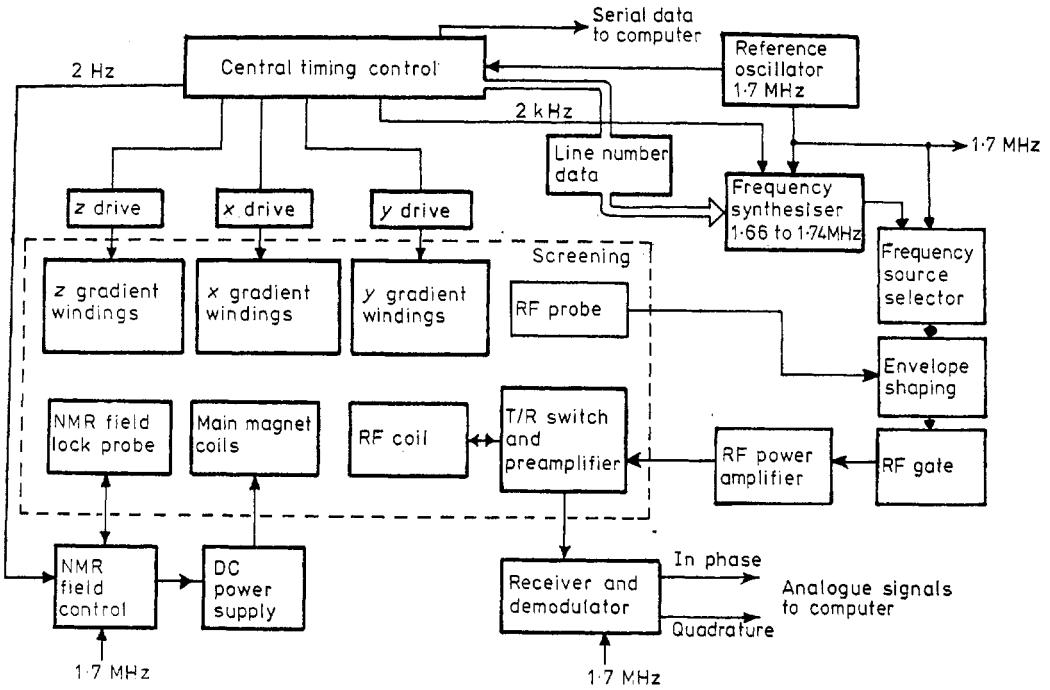

Figure 4 Block diagram of apparatus.

worth low pass filter (0 to 5 kHz) prior to being sampled at a data rate of 10 kHz using an LPS-11 computer interface.

4.2 RF *pulse envelope shaping*

To produce RF pulses of the required shape and size, we first generate a Gaussian waveform which is then used as a modulating signal. A linear ramp is integrated to produce a parabolic shape which is then converted to a Gaussian wave using the exponential relationship between collector current and base-emitter voltage in a transistor.

In our original design, the RF carrier was simply modulated by this Gaussian control waveform and passed to the rest of the amplifying and gating circuits, but it was found that the envelope of the resulting RF magnetic field applied to the sample was noticeably non-Gaussian. Secondly, the amplitude of the 180° pulse varied considerably with f_S despite the matching circuits (§4.4). Finally, inserting a patient reduces the Q factor of the RF coil which also affects the RF magnetic field.

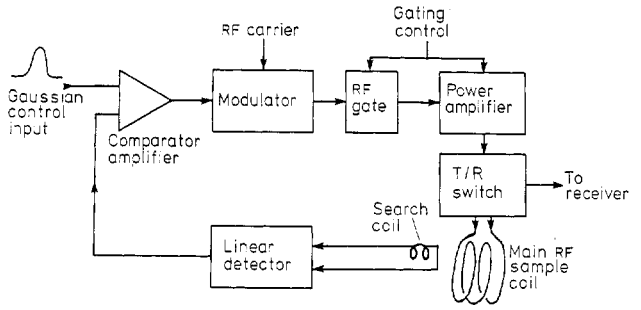

Figure 5 RF envelope feedback block diagram.

To overcome these nonlinear, frequency dependent and loading effects, envelope feedback was used as shown schematically in figure 5. The feedback search coil consists of ten turns on a 25 mm diameter former and is located under the patient couch. The induced voltage (2 V peak-to-peak for a 90° pulse) is fed directly to a linear detector whose output is compared with the Gaussian control waveform. The open loop frequency response changes somewhat with RF carrier frequency, which means that the high frequency roll-off in the comparator and modulator response must be carefully adjusted.

The Gaussian control waveform itself contains very few frequency components above 2 kHz so that the control loop can easily follow it, but the action of the isolating gates can create problems. Unless the Gaussian control input is driven slightly negative when the transmitter gates are off, the loop may drive the modulator fully on, resulting in a spike of RF when the gates are first opened.

4.3 RF *power amplifier*

It was estimated that a 100 W RF power amplifier would be adequate for the present application. Although commercial amplifiers are available, these are expensive and also lack certain useful features, such as the ability to gate off the amplifier output stage when no output is required. This not only reduces heat dissipation but minimises any noise sent to the transmit/receive switch during a signal collection period. We also require an amplifier that can drive a highly reactive load and appear as a high impedance source. This is not the case for a conventional amplifier with a 50 Ω output impedance.

With these points in mind, we designed and built an amplifier using VMOS (Siliconix Ltd) power semiconductors as shown in figure 6. Circuit design using these power MOSFET devices is straightforward. The only important point in layout is to keep the leads from the transistor drains to the output transformer as short and close together as possible to avoid RF current loops. The output stage is a class AB push-pull design with a quiescent current of about 70 mA per transistor; the peak drain current in any one transistor is 2 A.

The output transformer T_2 deserves mention in that it is 'pentafilar' wound; that is, five separate insulated wires are twisted together into a bundle which is then wrapped twice around the ferrite core (2 Mullard FX1105). Two of the wires are allocated to the primary and the other three connected in series to form the secondary. This form of construction virtually eliminates stray inductance, one of the biggest problems in high frequency transformers. The output has an impedance of over 500 Ω and effectively behaves as a current source.

The gating logic input is TTL compatible; when held at logic 0, all stages of the amplifier are cut off and no power is consumed. In practice, the amplifier is gated on for at most two bursts of 5 ms in each second, and no heating is evident.

4.4 *Transmit/receive switch*

We are using the same coil for applying the RF field to the sample and picking up the resultant signal. Even though our

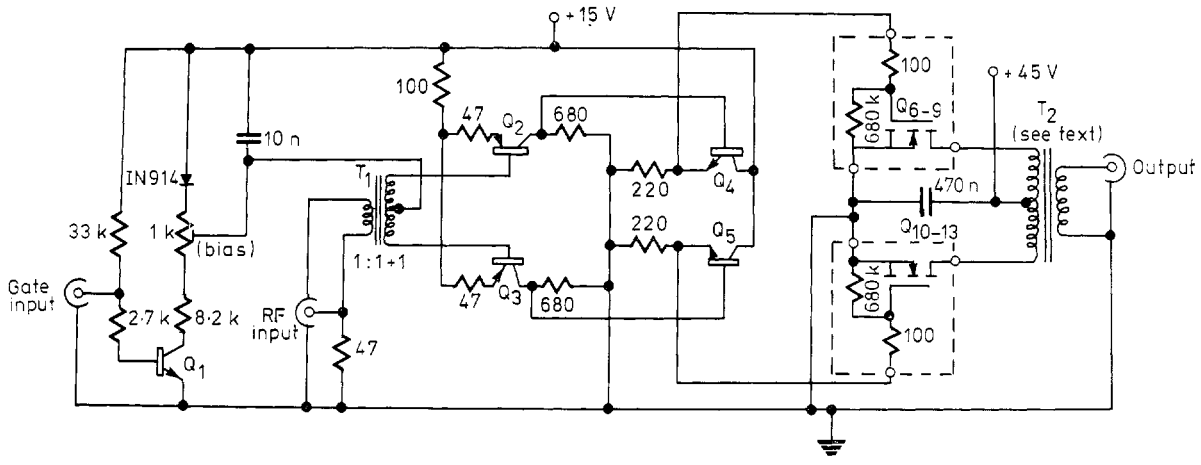

Figure 6 RF power amplifier. Transistors: Q_1, Q_4, Q_5, BC184L; Q_2, Q_3, BC214L; Q_6–Q_{13}, VN98AJ (Siliconix). Each box consists of four identical units in parallel.

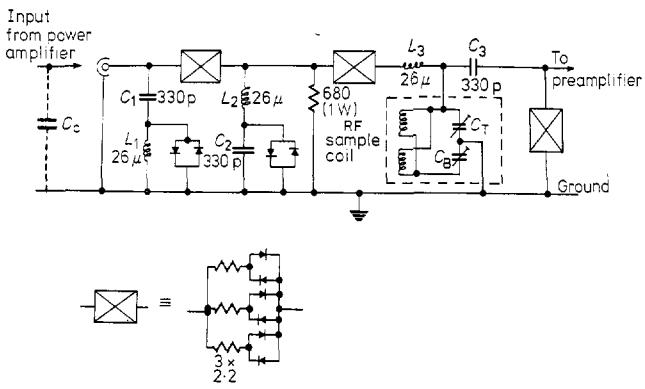

Figure 7 Transmit/receive switch. All diodes type 1N 4150.

applied RF magnetic field is a weak pulse with maximum strength 4×10^{-5} T, several hundred volts are required on the RF coil so that good isolation and protection is needed.

Figure 7 shows the circuit we use. Each inductance/capacitance pair (L_1 and C_1, L_2 and C_2, L_3 and C_3) is tuned to the operating frequency of 1·7 MHz.

When driven by the transmitter, all the crossed diode networks conduct and behave almost as short circuits; the whole circuit then acts as an impedance inverter. This is similar to the action of a quarter-wave transmission line which is sometimes used at higher frequencies. L_1 and C_2 are shorted out. L_2 and C_1 then form a parallel tuned circuit which presents a high impedance and thus does not load the transmitter significantly. C_c is the cable capacitance and in combination with L_3 and C_3 forms the impedance inverter. The input impedance

$$Z_{in} = \frac{L_3}{C_3 Z_L}$$

if

$$Z_L \gg Z_{in}$$

and

$$C_c \approx C_3,$$

where Z_L is the dynamic impedance of the RF sample coil. Since the RF coil is required to be driven at up to 40 kHz off resonance, Z_L and hence Z_{in} may be highly reactive. However, the impedance inversion function ensures that the RF voltage on the sample coil is reasonably independent of frequency if the transmitter acts as a current source.

In practice Z_{in} is about 15 Ω resistive at the centre frequency, 1·7 MHz, with an additional series reactance of up to 120 Ω at the frequency extremes, 1·66 and 1·74 MHz. The transmit/receive switch is connected to the transmitter by some 4 m of 50 Ω coaxial cable whose capacitance of 400 pF is slightly more than the optimum (330 pF).

In receive mode the crossed diodes no longer conduct but still exhibit a capacitance of about 15 pF for each block. However, L_1C_1 and L_2C_2 now behave as series resonators of low impedance, improving the isolation and filtering out any noise coming from the transmitter. The receiver pre-amplifier now sees the sample coil through C_3, whose reactance of 280 Ω is small enough to be unimportant.

4.5 *Receiver pre-amplifier*

Apart from providing low noise amplification, a major function of this unit is to damp the sample coil resonance sufficiently to give a reasonably flat response over the signal bandwidth of 10 kHz. If the coil was undamped, its Q factor of 400 would give a natural bandwidth of only 4·2 kHz, resulting in severe fall-off at the edges of each image line. A damped Q factor of less than 100 is desirable and could be achieved by straightforward resistive damping, but this would degrade the signal-to-noise figure substantially.

The design shown in figure 8 simulates a damping resistor of about 3 kΩ, but at very low effective temperature (< 20 K). An analysis of this principle and an example of another design is given by Hoult (1979). Our circuit is optimised for 1·7 MHz

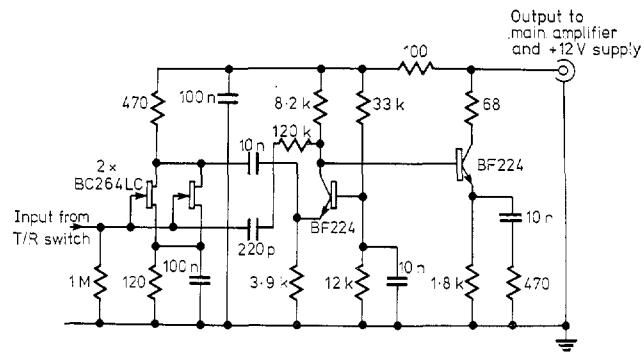

Figure 8 RF preamplifier.

and exhibits a noise figure of less than 1 dB for source resistances between 2 and 10 kΩ. It is also designed for remote operation inside the screened enclosure, and the power input and signal output share the same 50 Ω coaxial cable. The overall voltage gain is 3 with a 50 Ω load.

4.6 *Field gradient drivers*

Because of the requirement of large pulsed currents into an inductive load at a relatively low duty cycle, it was decided to design specialised thyristor based drivers.

4.6.1 *y gradient driver* To produce the desired axial gradient of 2·7 mT/m, the y gradient (slice selection) windings require a peak current of 40 A with a resultant back EMF of 320 V on the rising edge of the pulse. If a linear amplifier were used, its power handling capacity would have to be about 13 kW. However, the y gradient waveform is easily achieved by the capacitor discharge circuit shown in figure 9(*a*). During an unimportant part of the pulse sequence (in practice, at the beginning of interval 6 in figure 1, just after the signal collection period) $TRIG_1$ is pulsed to fire the triac TRC_1 and recharge C_1 to approximately V_0 volts.

When the y gradient pulse is required at the start of interval 3, $TRIG_2$ is pulsed to fire thyristor SCR_1. This causes C_1 to discharge into L_y, the gradient winding, in a resonant manner. The current through L_y builds up and decays as a half-cycle of a sine wave, but when it reverses sign, SCR_1 automatically turns off and the current flows through VR_1 and D_1. Thus, during the next (negative) half-cycle, VR_1 acts as a series damping resistance and can be adjusted so that the amplitude of this half-cycle is just that required for proper rephasing (interval 4).

At the end of this second half-cycle, the current again attempts to reverse sign but finds no pathway, so that all action stops and C_1 is left partially recharged; this is convenient from the viewpoint of power supply loading. The current waveform can be monitored by the potential drop across R_2.

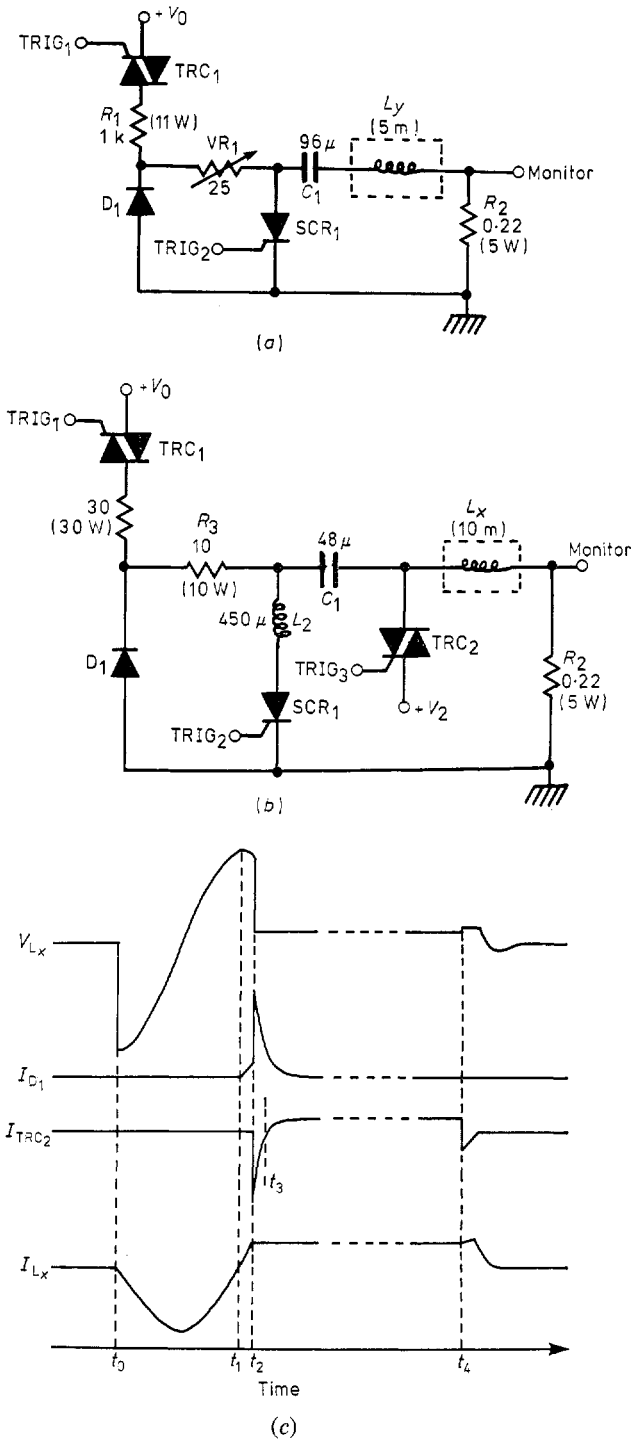

Figure 9 (*a*) *y* gradient driver. (*b*) *x* gradient driver. (*c*) *x* gradient waveforms.

SCR_1 is rated 600 V, 12 A continuous; although this would appear to be underrated, the 40 A pulse is well within its surge capabilities. Similar considerations apply to D_1. C_1 consists of a number of oil-filled block paper capacitors in parallel. The DC supply voltage V_0 can be pre-set anywhere from 250 to 500 V.

4.6.2 *z gradient driver* The *z* gradient (line selection) waveform is produced using a similar design philosophy, except that in this case a third harmonic is added to flatten the top of the waveform. The principle and the design are described more fully in a previous paper (Hutchison *et al* 1978). Since the *z* gradient winding has an inductance of only 370 μH, a series inductor was added to make the total inductance 10 mH, enabling us to use our resonant circuit. In this case the second half-cycle is of no importance and is allowed to proceed at maximum amplitude (VR_1 is replaced by a short circuit), thus recharging C_1 as much as possible and minimising power drain. Peak current into the load is 24 A.

4.6.3 *x gradient driver* The *x* gradient (readout) waveform consists of two distinct parts, a negative half-cycle and a long positive flat shown in figure 9(*c*). The driver circuit is shown in figure 9(*b*). The recharging of C_1 to V_0 volts and the production of the first half-cycle by pulsing $TRIG_2$ at time t_0 (see figure 1) is identical to the process for the *y* gradient. The second half-cycle, starting at t_1, is allowed to proceed until the current in L_x reaches that required for the flat portion of the waveform, at which time (t_2) the triac TRC_2 is fired by pulsing $TRIG_3$. This connects the winding to the low-voltage DC supply V_2 which maintains the current against the resistance of the winding.

The excess charge on C_1 is dissipated in R_3 through TRC_2 and D_1 and pulses current back into the supply V_2 until time t_3. This means that the gate drive to TRC_2 ($TRIG_3$) must be held active until after t_3 and secondly, that the V_2 power supply must be stabilised against the large pulse of reverse current; this is achieved by an electrolytic capacitor of 25 000 μF across the power supply output.

At the end of the observation period (t_4), $TRIG_1$ is pulsed to fire TRC_1. This causes current to flow through R_1, R_3 and C_1 which in turn attempts to reverse the current in TRC_2, thereby turning it off. Thereafter C_1 is recharged in the normal manner, thus completing the sequence.

A number of protection mechanisms have been incorporated into the *x* gradient driver. For example, V_0 must be present before V_2, and V_2 cuts out if loaded for more than 0·1 s continuously. L_2 is necessary to prevent destruction of the semiconductors in the event that SCR_1 does not turn off before TRC_2 fires; this could happen while adjusting the timing of $TRIG_3$ (t_2) during setting up.

As was the case for the *z* gradient, L_x consists of the gradient winding and a series inductor. V_0 is about 350 V and $V_2 = 16$ V. Peak negative current is 17 A and the flat readout portion needs 3 A. The timing of t_2 is fairly critical but is easily adjusted by observing the flatness of the readout portion of the current waveform at the point marked 'Monitor'.

5 System performance

In this section we discuss our method of data processing and experimental measurements of the image element characteristics. We also present some NMR phantom and *in vivo* human images, and a measurement of T_1 relaxation times of human tissues *in vivo*.

5.1 *Data processing*

The information for each image line consists of three complex signals, S_0, S_1 and S_2. The two components of these signals are each sampled at a 10 kHz rate, and 256 samples are collected and stored on a magnetic disc. Suitable averaging is performed for multiple scans, and a fast Fourier transform is done line by line yielding 40 lines of 256 points for a complete image. Each line is condensed into 64 points by averaging groups of four successive points.

Image displays are formed by interpolating the 40 lines of 64 points into 60 lines, which are embedded into a 64×64 matrix. Finally, this matrix is interpolated into a 128×128 array, and up to eight colours or grey tones are set at selected signal levels to give the image on a television monitor.

5.2 *Imaging element characteristics*

Consider the sensitive region corresponding to one of the 64 elements of one of the 40 image lines. To determine the shape and size of this element, a rectangular box about 50 mm × 50 mm in cross section, filled with $CuSO_4$ solution, was moved through the sensitive region in small steps and an edgespread function was obtained. These experimental points were then computer fitted to the integral of a Gaussian, the shape we expect from the form of our RF pulse.

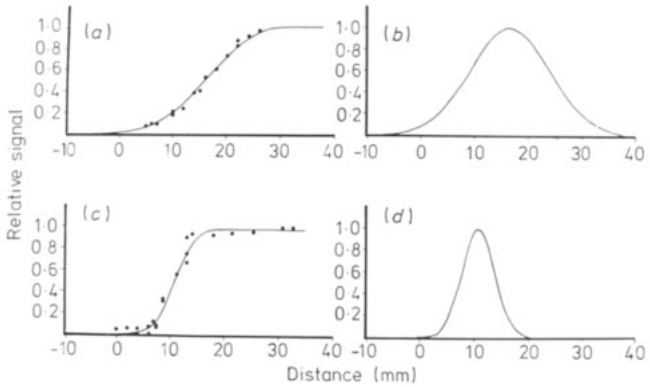

Figure 10 Imaging element lineshape. (*a*) measured *y* edgespread function and (*b*) derived *y* linespread function with equivalent rectangular width 18·5 mm. (*c*) measured *z* edgespread function and (*d*) derived *z* linespread function with equivalent rectangular width 7·5 mm.

The experimental data, fitted line and Gaussian linespread function derived for the *y* and *z* dimensions of the imaging element are shown in figure 10. The *x* dimension of the element is determined by the number of points averaged from the Fourier transform. The *x* linespread function is therefore rectangular, with width 7·4 mm in our case. So each imaging element is about 7·5 mm high, 7·4 mm wide, and 18·5 mm thick, giving a volume of 10^3 mm^3. The line separation is 12 mm.

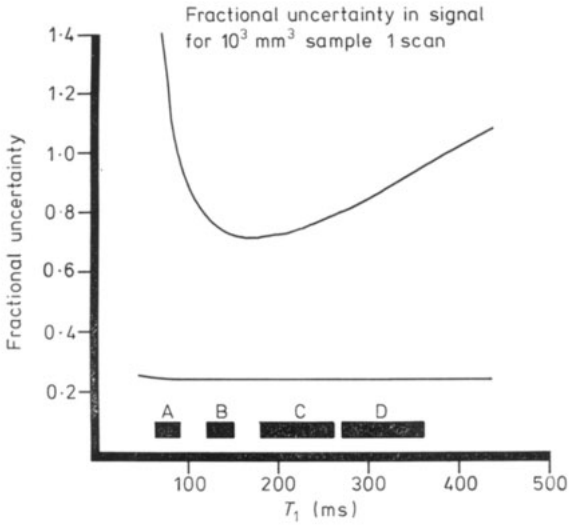

Figure 11 **Proton density resolution and T_1 resolution.** The horizontal bars along the T_1 axis show the approximate ranges of T_1 for the following tissues: A, white bone marrow and mesentery; B, liver; C, muscle; D, lung and brain.

5.3 *Proton density resolution and* T_1 *resolution*

Of crucial importance in the quality of images we can produce are the uncertainties in the proton density and T_1 values in each imaging element. The curves in figure 11 are derived from experimental measurements and indicate the resolution obtained in a single scan through a 10^3 mm^3 volume of human muscle tissue *in vivo*. Our whole-body images are derived from four single scans taking 8 min in all. We can infer from figure 11 that in this case the uncertainty in proton density should be 12% and the uncertainty in T_1 approximately 37% with some worsening as T_1 departs from the optimum value of around 200 ms. Although the proton density resolution is better than that for T_1, water content varies less than 20% among soft tissues whereas the T_1 variation can be very much greater. Figure 11 shows some typical T_1 ranges obtained from excised animal tissues at 2·5 MHz (Ling *et al* 1980).

5.4 *Images*

Figure 12 shows the image of a square array of bottles containing $CuSO_4$ solution. Lighter shades of grey correspond

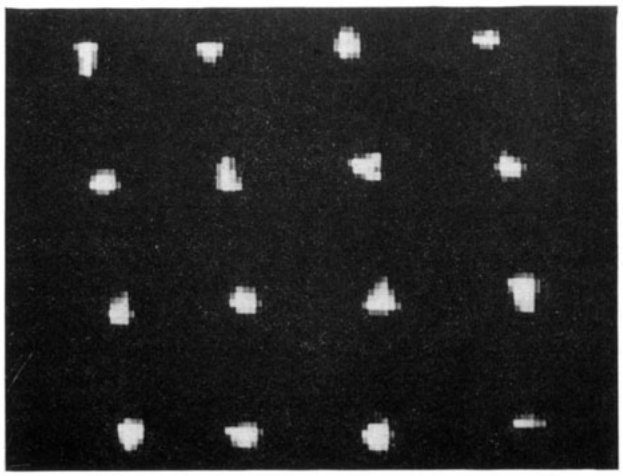

Figure 12 Proton density image of square array of bottles containing $CuSO_4$ solution.

to increasing proton density. The bottles are each 20 mm in diameter and are spaced 75 mm apart in a square lattice. The slight skewness in the image is a consequence of small non-uniformities in our magnetic fields.

Figure 13 illustrates how we can produce T_1 images from our data. Two 50 mm × 50 mm cross section plastic boxes were filled with $CuSO_4$ solution having T_1 about 200 ms and 400 ms respectively. The first row in the figure shows a proton density image (using S_A only) along with a line profile through the boxes; the images and signal heights are similar. The second shows the S_B signal, which is strongly dependent on T_1, and the left hand box has a larger S_B and hence longer T_1. The third row shows an image constructed from the calculated T_1.

Figure 14 shows a whole-body, proton density transverse section through the chest of one of the authors (JMSH), and again lighter tones correspond to increasing proton density. This image and those following took 8 min to produce and are averages of four single images. The arms, lungs, heart and chest wall are clearly visible. There is an obvious artifact, an extraneous signal aligned with the heart, which is caused by heart motion. This is a consequence of our subtractive method of obtaining S_A and S_B, and work is proceeding on new

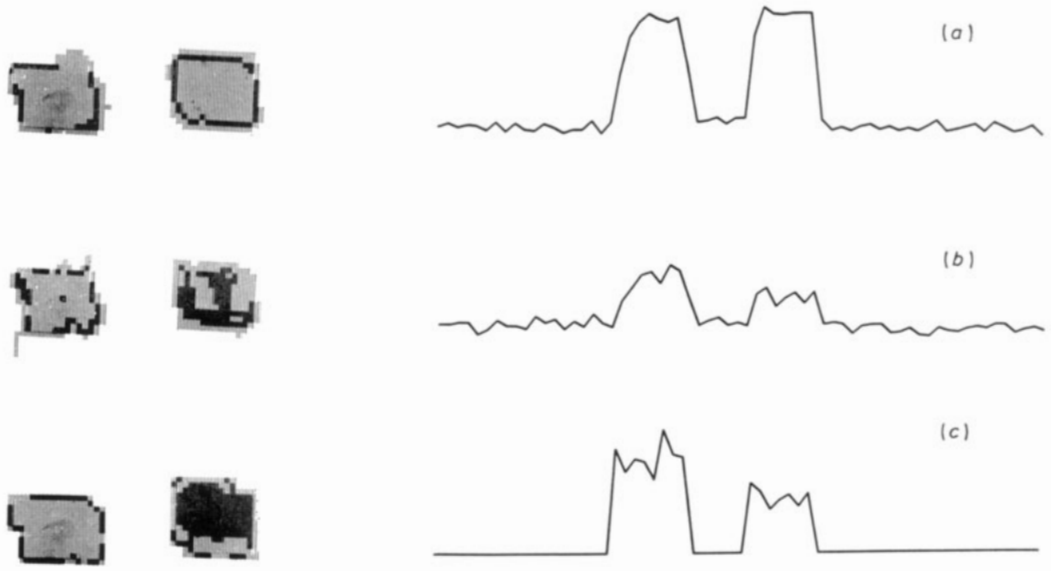

Figure 13 Images of boxes containing $CuSO_4$ solutions with different T_1's. (*a*) proton density image. (*b*) S_B image. (*c*) Image derived from T_1's calculated for each imaging element.

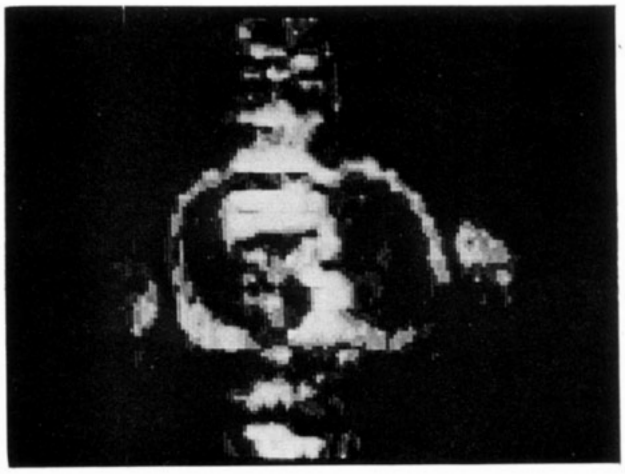

(*a*)

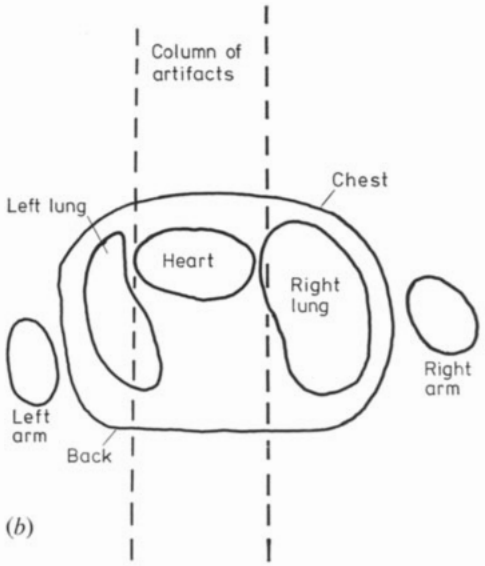

(*b*)

Figure 14 (*a*) Proton density thorax image. (*b*) Outline of important features in thorax image.

methods which should alleviate this problem. Largely because of this difficulty, our whole-body T_1 images have not been successful.

Figure 15 shows a transverse section through the head of JMSH taken about 40 mm above the eyes, with the anterior side to the right; the two hemispheres are clearly separated.

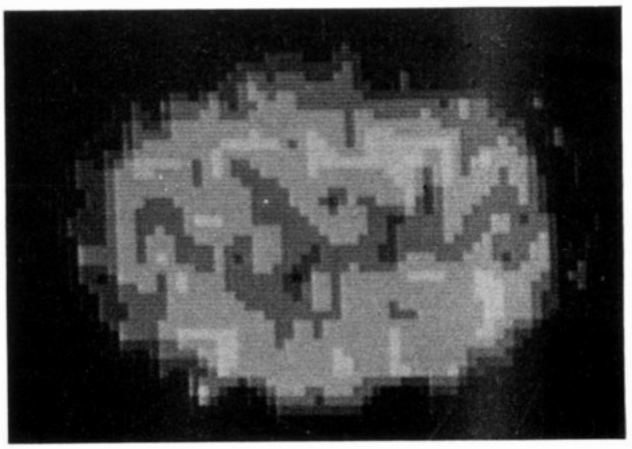

Figure 15 Proton density head image.

Figure 16 is a transverse section through the thighs of JMSH; the femurs are readily visible and there is an indication of bone marrow.

5.5 In vivo T_1 *measurements*

Although our machine cannot yet produce acceptable whole body T_1 images, it proved possible to use it to make T_1 measurements of various human tissues *in vivo*. The procedure is to take a complete proton density image and choose a line in a particular region of the tissue involved. We then collect 16 sets of signals from that line, which takes 48 s. The data over a selected length of about 75 mm is then averaged and T_1

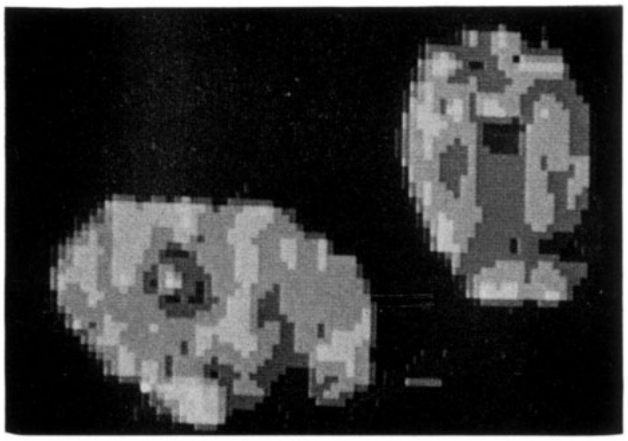

Figure 16 Proton density thigh image.

calculated. This is done for muscle, liver and brain tissue using scans through the thigh, abdomen and head.

The results are given in table 1. The first two columns show our human *in vivo* T_1 values for two experiments on JMSH. Each experiment consisted of five runs with JMSH in position. The two experiments were done on separate occasions to check reproducibility. The third column shows measurements on rabbit tissues *in vitro* at 2·5 MHz (Ling *et al* 1980), and the

Table 1 **Human *in vivo* T_1 measurements.**

	Human *in vivo* (1·7 MHz)		Rabbit *in vitro*
	Experiment 1	Experiment 2	(2·5 MHz)
Muscle	200 ± 6	215 ± 5	182 ± 14
Liver	143 ± 10	143 ± 13	141 ± 16
Brain	250 ± 10	303 ± 10	298 ± 30

agreement with the human tissue values is good. The different human brain values might be explained by the quite different T_1 values of white and grey brain tissue (e.g. Go and Edzes 1975). This experiment supports the validity of T_1 measurements *in vitro* of animal tissues and their applicability to human imaging *in vivo*.

6 Conclusion

We have constructed an NMR system to make tomographic images of the whole human body, and some images have been produced. The machine has been used to measure T_1 relaxation times of several human tissues *in vivo*, and the results indicate that relaxation time measurements in excised animal tissues are applicable to human imaging.

In its present form our machine is only a beginning. However, the imaging parameters we have measured indicate that the implementation of faster information gathering techniques (e.g. Kumar *et al* 1975, Mansfield and Pykett 1978) should lead to practical systems which will produce significant discrimination among various human tissues in whole-body, *in vivo* images.

Acknowledgments

We acknowledge the financial support of the University of Aberdeen and the Medical Research Council under grant N975/937. We thank Professor J R Mallard for his encouragement and assistance and Mr T Redpath for helpful comments on the manuscript.

References

Damadian R, Goldsmith M and Minkoff L 1977 NMR in Cancer: XVI. Fonar image of the live human body *Physiol. Chem. Phys.* **9** 97–100

Go K G and Edzes H T 1975 Water in brain edema: observations by pulsed NMR *Arc. Neurol.* **32** 462–5

Hinshaw W S 1976 Image formation by nuclear magnetic resonance: the sensitive point method *J. Appl. Phys.* **47** 61–5

Holland G N, Moore W S and Hawkes R C 1980 NMR tomography of the brain *J. Computer Assisted Tomography* **4** 1

Hoult D I 1978 Rotating frame zeugmatography *J. Magn. Resonance* **33** 183–97

Hoult D I 1979 Fast recovery, high sensitivity NMR probe and pre-amplifier for low frequencies *Rev. Sci. Instrum.* **50** 193–200

Hutchison J M S 1976 Imaging by nuclear magnetic resonance *Proc. 7th L H Gray Conf. on Medical Images, Leeds* (Bristol, Inst. of Physics: Wiley) 135–41

Hutchison J M S, Sutherland R J and Mallard J R 1978 NMR imaging: image recovery under magnetic fields with large non-uniformities *J. Phys. E: Sci. Instrum.* **11** 217–21

Hutchison J M S, Sutherland R J, Edelstein W A and Mallard JR 1979 Field gradient coils *UK patent 7934864*

Kumar A, Welti D and Ernst R R 1975 NMR Fourier Zeugmatography *J. Magn. Resonance* **18** 69–83

Lauterbur P 1973 Image formation by induced local interactions: examples employing nuclear magnetic resonance *Nature* **242** 190

Ling C R, Foster M A and Hutchison J M S 1980 Comparison of NMR water proton T_1 relaxation times of rabbit tissues at 24 MHz and 2·5 MHz *Phys. Med. Biol.* **25** 748–51

Mallard J R, Hutchison J M S, Edelstein W A, Ling C R, Foster M A and Johnson G 1980 *In vivo* NMR imaging in medicine: the Aberdeen approach, both physical and biological *Phil. Trans. R. Soc. London B* **289** 519–30

Mansfield P, Maudsley A A and Baines T 1976 Fast scan proton density imaging by NMR *J. Phys. E: Sci. Instrum.* **9** 271–8

Mansfield P and Pykett I L 1978 Biological and medical imaging by NMR *J. Magn. Resonance* **29** 69–83

Mansfield P, Pykett I L and Morris P G 1978 Human whole body line-scan imaging by NMR *Brit. J. Radiol.* **51** 921–2

Sutherland R J and Hutchison J M S 1978 Three-dimensional NMR imaging using selective excitation *J. Phys. E: Sci. Instrum.* **11** 79–83